

Spin-torsion dominated hyperfine splittings in the first excited torsional state ($\nu_t = 1$) of methanol

Li-Hong Xu^a, J.T. Hougen^{b,*}, G.Yu. Golubiatnikov^c, S.P. Belov^c, A.V. Lapinov^c, E.A. Alekseev^{d,e}, I. Krapivin^d, L. Margulès^f, R.A. Motiyenko^f, S. Bailleux^f

^a Department of Physics and Centre for Laser, Atomic, and Molecular Sciences, University of New Brunswick, Saint John, NB E2L 4L5, Canada

^b Scientist Emeritus, Sensor Science Division, National Institute of Standards and Technology, Gaithersburg, MD 20899-8441, USA

^c Institute of Applied Physics of the Russian Academy of Sciences, 46 Ulyanov Street, 603950 Nizhny Novgorod, Russia

^d Institute of Radio Astronomy of the National Academy of Sciences of Ukraine (IRA NASU), 4, Mystetstv St., Kharkiv 61002, Ukraine

^e Quantum Radiophysics Department of V.N. Karazin Kharkiv National University, Svobody Square 4, Kharkiv 61002, Ukraine

^f Laboratoire de Physique des Lasers, Atomes, et Molécules, UMR CNRS 8523, Université de Lille I, 59655 Villeneuve d'Ascq Cedex, France

ARTICLE INFO

Article history:

Received 18 October 2018

In revised form 14 December 2018

Accepted 18 December 2018

Available online 21 December 2018

Keywords:

Effective Hamiltonian

First excited torsional E state

Least-squares fit

Magnetic hyperfine structure

Methanol

Spin-rotation interaction

Spin-torsion interaction

ABSTRACT

Doublet, triplet and quartet hyperfine splitting patterns have been observed in the E-species component of the first excited ($\nu_t = 1$) torsional state of CH_3OH . Four series of lines dominate the available data: (i) a $K = 6 \leftarrow 7$, Q branch series of quartets, with $7 \leq J \leq 15$; (ii) a $K = 3 \leftarrow 2$, Q branch series, with $3 \leq J \leq 18$, which starts as quartets, changes to doublets at $J = 7$, and then finally to singlets at $J = 17$; (iii) a $K = -2 \leftarrow -3$, P branch series of doublets, with $8 \leq J \leq 13$; and (iv) a $K = 8 \leftarrow 7$, Q branch series, with $8 \leq J \leq 24$, which starts as triplets and becomes doublets at $J = 12$. There are also a few isolated doublets and quartets, which do not form long spectroscopic branches. We have modeled the hyperfine quartet and doublet splittings with empirically chosen symmetry-allowed spin-torsion, spin-rotation, and spin-spin interaction terms appropriate for the two $I = \frac{1}{2}$ spin systems arising from the OH proton and from the CH_3 protons, respectively, and have achieved a least-squares fit of 144 hyperfine components (88 hyperfine intervals) to six hyperfine parameters with a standard deviation (0.75 kHz) near experimental measurement accuracy. The three spin-rotation parameters associated with one $I = \frac{1}{2}$ spin system in the fit agree well with ab initio predictions for I_{OH} parameters in the literature. The two spin-torsion parameters agree to some extent with other fitted values in the literature. The physical effects included in the present Hamiltonian differ from those included in the Hamiltonian for our earlier work on hyperfine splittings in $\nu_t = 0$ E states, because the experimentally observed $\nu_t = 1$ splittings are found to decrease approximately as $1/J$, whereas the $\nu_t = 0$ splittings increase approximately as J . The position and relative intensities of the weak central features of the triplets are explained as three-level Λ -type crossover resonances.

© 2018 Elsevier Inc. All rights reserved.

1. Introduction

Extensive Lamb-dip measurements of hyperfine splitting patterns in methanol in the submillimeter and microwave spectral regions began about five years ago in Nizhny Novgorod, Russia [1], and then gradually spread to Kharkov, Ukraine and Lille, France. Observed splittings lie in the range of 20–200 kHz, and many of the corresponding hyperfine components are clearly resolved under the available instrumental resolution of about 20 kHz. The nuclear spins in normal CH_3OH have the values

$I_{\text{C}} = I_{\text{O}} = 0$ and $I_{\text{H}} = \frac{1}{2}$, so that these hyperfine splittings must arise only from nuclear magnetic dipole effects (e.g., spin-rotation, spin-torsion, and spin-spin interactions, represented here by the Hamiltonians H_{sr} , H_{st} , and H_{ss}), and not from electric quadrupole effects.

Two different types of theoretical treatment have been used in the literature to treat portions of the observed data. The first [2,3] involves using quantum chemistry packages to first calculate ab initio values for the approximately 60 interaction constants in H_{sr} and H_{ss} , as well as some contributions to the approximately 15 interaction constants in H_{st} . Because of the limited number of hyperfine splittings experimentally available, most of these computed constants must be kept fixed, with only a judiciously chosen small set varied in any fit to experimental data. The second

* Corresponding author at: Sensor Science Division, NIST, 100 Bureau Drive, Gaithersburg, MD 20899-8441, USA.

E-mail address: jon.hougen@nist.gov (J.T. Hougen).

approach [4], involves relying on intuition, symmetry arguments, and trial-and-error procedures to construct an effective hyperfine Hamiltonian H_{eff} , containing the minimum number of interaction terms required to fit the data.

In previous work [4] we used an effective Hamiltonian with matrix elements connecting the two components of degenerate torsion-rotation E states to fit hyperfine doublet splittings in the $\nu_t = 0$ torsional ground state of methanol. The torsionally mediated spin-rotation interaction terms used in that work only exist in molecules with an internal rotor. In the present work we extend our study to hyperfine splittings in the first excited ($\nu_t = 1$) torsional state of methanol, where spin-torsion interactions are expected to become much larger.

The data set considered is discussed in Section 2. The basic theory used to construct the effective hyperfine Hamiltonian is discussed in Section 3. Assignment ambiguities and least-squares fits of the data to the theory are presented in Sections 4 and 5. In Section 6, we compare our fitted hyperfine coupling constants with both theoretical and experimental values in the literature. In Section 7 we give possible explanations for the weak central components in some of our observed hyperfine patterns. Section 8 presents conclusions.

2. The $\nu_t = 1$ E-species data set

Previously existing data from Nizhny Novgorod and Kharkov on the methanol Lamb-dip spectra were supplemented in this work by new measurements carried out recently in Lille at frequencies from 210 to 330 GHz. A general description of the Lille spectrometer may be found in [5]. To provide sub-Doppler resolution, the spectrometer in [5] was modified according to a commonly used approach, where a roof-top mirror is used to rotate the polarization by 90° at one end of the absorbing cell, and a wire-grid polarizer is used to separate the backward and forward waves at the other end. The spectrometer operates with a frequency modulated radiation source and a second harmonic lock-in detection system. To minimize possible line-shape distortions, the modulation frequency was as small as 2.5 kHz, with a modulation depth of about 12 kHz.

Our E-species measurements in the $\nu_t = 1$ torsional state of methanol can be divided into four categories, according to whether the observed hyperfine pattern for any given torsion-rotation transition is a quartet, triplet, doublet, or singlet. They can also be classified in another way, according to whether a given hyperfine pattern can be grouped together with other observed patterns belonging to the same P, Q or R branch in the spectrum (i.e., to a branch defined by given upper-state K' and lower-state K'' quantum numbers, with increasing J values), or whether the hyperfine pattern belongs to an isolated torsion-rotation transition in the measured data set.

Using these criteria, the observed data set can be described as follows. There are four series of lines belonging to the following spectral branches: (i) a $K = 6 \leftarrow 7$ Q branch measured in Lille [5], with J from 7 to 15, where quartet hyperfine splitting patterns are observed for all J transitions; (ii) a $K = 3 \leftarrow 2$ Q branch measured in Nizhny Novgorod [6], with J from 3 to 18, which starts off as quartets, changes to doublets at $J = 7$, and then changes to singlets at $J = 17$; (iii) a $K = -2 \leftarrow -3$ P branch measured in Nizhny Novgorod [6], with $J'' = 8$ and 10 to 13, where doublets are observed for all J values; and (iv) a $K = 8 \leftarrow 7$ Q branch measured in Lille [5], with J from 8 to 24, where the series starts off as triplets with a weak central component, and then apparently changes to doublets at $J = 12$. There are 11 other $\nu_t = 1$ E lines with clear hyperfine splittings.

Measurement precision for splittings in the good lines is thought to be between 0.5 and 1 kHz, although confirmation of this

estimate by combination differences is not possible. One hyperfine doublet was measured in two laboratories, however, namely that for the $\nu_t = 1$ $J_{KaKc} = 2_{02} \leftarrow 1_{11}$ rotational transition. The measurements from Nizhny Novgorod are 286 182.344 and 286 182.385 MHz, giving a hyperfine splitting of 41 kHz. The measurements from Lille are 286 182.3396 and 286 182.3815 MHz, giving a hyperfine splitting of 41.9 kHz. (Note that absolute frequencies were not carefully determined in either laboratory, because only hyperfine splittings between close lying lines are of interest in this study.) Table 1 contains a list of the measured hyperfine transitions and their quantum number assignments.

3. Basic theory used to set up H_{eff}

3.1. Spin-rotation interaction

The theory for H_{sr} below comes mostly from Section S-III of the Supplementary Material to Ref. [4], with slight changes in notation. We write

$$H_{\text{sr}} = C_{\text{sr}}^{\text{OH}} (\mathbf{I}_{\text{OH}} \cdot \mathbf{J})_{\text{LAB}} + C_{\text{sr}}^{\text{CH}_3} (\mathbf{I}_{\text{CH}_3} \cdot \mathbf{J})_{\text{LAB}}, \quad (1)$$

where $C_{\text{sr}}^{\text{OH}}$ and $C_{\text{sr}}^{\text{CH}_3}$ are interaction constants depending on rotational and torsional quantum numbers as defined further below, \mathbf{I}_{OH} and \mathbf{I}_{CH_3} represent the $I = 1/2$ nuclear spin systems arising from the hydroxyl proton and from the three methyl protons in a torsional state of E symmetry, \mathbf{J} is the rotational angular momentum of the CH₃OH molecule, and the subscript LAB indicates that the dot products are to be formed from components of the vector operators in the laboratory-fixed axis system.

The form of the coefficients $C_{\text{sr}}^{\text{OH}}$ and $C_{\text{sr}}^{\text{CH}_3}$ depends on the spin-rotation operators they contain. Table 1 of [4] gives a recipe for generating all possible symmetry-allowed spin-rotation operators in methanol from molecule-fixed components of \mathbf{I}_{OH} , \mathbf{I}_{CH_3} , and \mathbf{J} . Eqs. (16) and (17) of [4] considered particularly simple linear combinations of such operators. Our preliminary calculations have shown that for the $\nu_t = 1$ transitions of E symmetry considered here, CH₃ proton-spin operators of the forms $\mathbf{I}_{\text{EA}1}$ and $\mathbf{I}_{\text{EA}2}$, that were important in Eq. (20) of [4], are not important here, and only CH₃ proton-spin operators of the form $\mathbf{I}_{\text{A}1}$ (as in Eq. (16) of [4]) give large contributions to the observed hyperfine splittings. We in fact consider only three of the five possible terms for each spin system (\mathbf{I}_{CH_3} and \mathbf{I}_{OH}), namely those of the form I_{Jx} , I_{Jy} , and I_{Jz} , but we regroup them and write (in a notation analogous to Eqs. (23) and (24) of [4]):

$$C_{\text{sr}}^{\text{OH}} = \left[C_{\text{zz}}^{\text{OH}} \langle J_z^2 \rangle + C_{\text{xx-yy}}^{\text{OH}} (\langle J_x^2 \rangle - \langle J_y^2 \rangle) + C_{\text{xx+yy+zz}}^{\text{OH}} \langle J^2 \rangle \right] / J(J+1) \quad (2a)$$

$$C_{\text{sr}}^{\text{CH}_3} = \left[C_{\text{zz}}^{\text{CH}_3} \langle J_z^2 \rangle + C_{\text{xx-yy}}^{\text{CH}_3} (\langle J_x^2 \rangle - \langle J_y^2 \rangle) + C_{\text{xx+yy+zz}}^{\text{CH}_3} \langle J^2 \rangle \right] / J(J+1). \quad (2b)$$

The six C coefficients on the right side of Eq. (2) will be determined by a least-squares fit to the experimental hyperfine splitting patterns. The three expectation values in brackets $\langle \rangle$ are calculated from torsion-rotation wavefunctions given in an earlier paper [7], using a procedure similar to that described in Section V.B of [4], except that the expectation values in the present work are all calculated within the $|^{\text{tr}}E_+\rangle$ component of the appropriate torsion-rotation states, and thus have the form

$$\langle J_z^2 \rangle = \langle ^{\text{tr}}E_+ | J_z^2 | ^{\text{tr}}E_+ \rangle \approx K^2 \quad (3a)$$

$$\langle J_x^2 - J_y^2 \rangle = (1/2) \langle ^{\text{tr}}E_+ | J_+^2 + J_-^2 | ^{\text{tr}}E_+ \rangle \sim J^4 \quad (3b)$$

$$\langle J^2 \rangle = \langle ^{\text{tr}}E_+ | J^2 | ^{\text{tr}}E_+ \rangle \equiv J(J+1). \quad (3c)$$

Table 1

Submillimeter Lamb-dip measurements^a of hyperfine components of $v_t = 1$ torsion-rotation transitions of E species in methanol, together with their J , K , F and F_1 ^b quantum number assignments.

Series (i) in Section 2: $K' \leftarrow K'' = +6 \leftarrow +7$, $Q(J'')$ transitions							
	$F = J \ (F_1 = J + \frac{1}{2})$	$F = J + 1 \ (F_1 = J + \frac{1}{2})$	$F = J - 1 \ (F_1 = J - \frac{1}{2})$	$F = J \ (F_1 = J - \frac{1}{2})$			
$J'' = 7$	232422.8651	232422.9246	232423.0293	232423.0846			
$J'' = 8$	232645.1674	232645.2193	232645.3102	232645.3586			
$J'' = 9$	232847.1598	232847.2049	232847.2891	232847.3319			
$J'' = 10$	233011.9239	233011.9654	233012.0405	233012.0791			
$J'' = 11$	233121.1927	233121.2295	233121.2992	233121.3336			
$J'' = 12$	233155.8918	233155.9264	233155.9899	233156.0219			
$J'' = 13$	233096.8055	233096.8365	233096.8950	233096.9247			
$J'' = 14$	232925.4163	232925.4454	232925.4991	232925.5275			
$J'' = 15$	232624.7720	232624.7980	232624.8500	232624.8760			
Series (ii) in Section 2: $K' \leftarrow K'' = +3 \leftarrow +2$, $Q(J'')$ transitions (some measurements available only to 3 decimal digits)							
	$F = J \ (F_1 = J - \frac{1}{2})$	$F = J - 1 \ (F_1 = J - \frac{1}{2})$	$F = J + 1 \ (F_1 = J + \frac{1}{2})$	$F = J \ (F_1 = J + \frac{1}{2})$			
$J'' = 3$	365046.8762	365046.9220	365047.0422	365047.0976			
$J'' = 4$	365030.918	365030.954	365031.046	365031.087			
$J'' = 5$	364986.741	364986.772	364986.845	364986.880			
$J'' = 6$	364898.237	364898.264	364898.324	364898.353			
	$F = JJ - 1 (F_1 = J - \frac{1}{2})$			$F = JJ + 1 (F_1 = J + \frac{1}{2})$			
$J'' = 7$	364746.142			364746.221			
$J'' = 8$	364508.067			364508.137			
$J'' = 9$	364158.694			364158.756			
$J'' = 10$	363669.901			363669.956			
$J'' = 11$	363011.028			363011.076			
$J'' = 12$	362149.215			362149.260			
$J'' = 13$	361049.838			361049.879			
$J'' = 14$	359676.996			359677.033			
$J'' = 15$	357994.137			357994.170			
$J'' = 16$	355964.693			355964.723			
Series (iii) in Section 2: $K' \leftarrow K'' = -2 \leftarrow -3$, $P(J'')$ transitions (measurements available only to 3 decimal digits)							
	$F = JJ - 1 (F_1 = J - \frac{1}{2})$			$F = JJ + 1 (F_1 = J + \frac{1}{2})$			
$J'' = 8$	488945.451			488945.484			
$J'' = 10$	392529.159			392529.186			
$J'' = 11$	344312.235			344312.260			
$J'' = 12$	296084.094			296084.117			
$J'' = 13$	247840.037			247840.058			
Series (iv) in Section 2: $K' \leftarrow K'' = +8 \leftarrow +7$, $Q(J'')$ transitions							
	$F = JJ + 1 (F_1 = J + \frac{1}{2})$			$F = JJ - 1 (F_1 = J - \frac{1}{2})$			
$J'' = 8$	292864.1859			292864.2933			
$J'' = 9$	293051.2374			293051.3328			
$J'' = 10$	293330.6729			293330.7590			
$J'' = 11$	293724.5130			293724.5910			
$J'' = 12$	294255.9490			294256.0220			
$J'' = 13$	294948.6864			294948.7530			
$J'' = 14$	295826.0925			295826.1538			
$J'' = 15$	296910.3244			296910.3807			
$J'' = 16$	298221.5148			298221.5676			
$J'' = 17$	299777.0812			299777.1313			
$J'' = 18$	301591.3066			301591.3532			
$J'' = 19$	303675.1963			303675.2402			
$J'' = 20$	306036.6414			306036.6841			
$J'' = 21$	308680.7905			308680.8303			
$J'' = 22$	311610.5592			311610.5978			
$J'' = 23$	314827.2129			314827.2483			
$J'' = 24$	318330.9147			318330.9503			
Transitions not falling in series							
J'	K'	J''	K''	$F = J \ (F_1 = J + \frac{1}{2})$	$F = J + 1 \ (F_1 = J + \frac{1}{2})$	$F = J - 1 \ (F_1 = J - \frac{1}{2})$	$F = J \ (F_1 = J - \frac{1}{2})$
9	6	10	7	-249003.9321	-249003.8934	-249003.8094	-249003.7709
10	6	11	7	-296967.6646	-296967.6300	-296967.5532	-296967.5190
3	3	2	2	$F = J \ (F_1 = J - \frac{1}{2})$ 509780.1062	$F = J - 1 \ (F_1 = J - \frac{1}{2})$ 509780.1600	$F = J + 1 \ (F_1 = J + \frac{1}{2})$ 509780.3088	$F = J \ (F_1 = J + \frac{1}{2})$ 509780.3644
J'		K'	J''		K''	$F = JJ - 1 (F_1 = J - \frac{1}{2})$	$F = JJ + 1 (F_1 = J + \frac{1}{2})$
11		3	12		2	-215691.8212	-215691.7713
2		0	1		1	286182.344	286182.385
1		0	2		1	93196.660	93196.686

(continued on next page)

Table 1 (continued)

J'	K'	J''	K''	$F = J'J - 1(F_1 = J - 1/2)$	$F = J'J + 1(F_1 = J + 1/2)$
3	−2	2	−2	$F = J'J + 1(F_1 = J + 1/2)$ 144728.758	$F = J'J - 1(F_1 = J - 1/2)$ 144728.783
3	2	2	2	$F = J'J - 1(F_1 = J - 1/2)$ 144733.230	$F = J'J + 1(F_1 = J + 1/2)$ 144733.265
2	−1	1	−1	96501.6741	96501.7174
17	3	18	4	250969.9526	250969.9699
1	0	1	1	189688.805	189688.845

^a Absolute frequencies of each hyperfine component are estimated to have a relative uncertainty of 0.5 to 1 kHz (type B, coverage $k = 1$ [10]). There are more Q branches than R and P branches in this measurement table because of the large value of $B + C \approx 48.5$ GHz for methanol.

^b F_1 labels are indicated in parentheses.

The expectation value in Eq. (3a) was found in many cases to be quite near the square of the symmetric-top K value for the $|^rE_+ \rangle$ state under consideration. The expectation value in Eq. (3b) starts at zero when $J = K$, but increases rapidly as J increases. The empirical J^4 dependence comes from the fact that plots of $\log \langle J_z^2 \rangle$ vs $\log(J)$ for the $\langle J_z^2 \rangle$ expectation values in Table S-1 of the supplementary material all have an approximate slope of four. This can be understood semi-quantitatively as follows. (i) Expectation values of $\langle J_z \rangle$ are nearly equal to a signed-integer K value for all the eigenfunctions considered in Table S-1, so that signed K is nearly a good quantum number for these $v_t = 1$ E-species eigenfunctions. (ii) Non-zero matrix elements of J_z^2 in the basis set obey $\Delta K = -2$ selection rules and are approximately proportional to J^2 . (iii) The small $\Delta K = \pm 2$ mixing coefficients for basis functions in the final eigenfunctions are also proportional to J^2 , whether they arise from two consecutive $\Delta K = \pm 1$ mixings (e.g., via D_{ab}), or from one $\Delta K = \pm 2$ mixing (e.g., via $B-C$). The product of the J^2 dependence of basis-set matrix elements and the J^2 dependence of basis-set mixing coefficients then gives an overall J^4 dependence for expectation values calculated using eigenfunctions. The expectation value in Eq. (3c) is, of course, always exactly equal to $J(J+1)$, since J is a good quantum number in the torsion-rotation problem.

3.2. Spin-torsion interaction

These operators were not used in the data treatment of [4], but they can be generated from Table 1 there by noting that the symmetry properties of P_α are the same as those of J_z . We consider only half the possible spin-torsion terms, namely those of the form $I_z P_\alpha$, and write, analogous to Eqs. (1)–(3) for the spin-rotation interaction,

$$H_{st} = C_{st}^{OH} (\mathbf{I}_{OH} \cdot \mathbf{J})_{LAB} + C_{st}^{CH3} (\mathbf{I}_{CH3} \cdot \mathbf{J})_{LAB}, \quad (4)$$

where

$$C_{st}^{OH} = C_{\alpha\alpha}^{OH} \langle P_\alpha J_z \rangle / J(J+1) \quad (5a)$$

$$C_{st}^{CH3} = C_{\alpha\alpha}^{CH3} \langle P_\alpha J_z \rangle / J(J+1) \quad (5b)$$

and

$$\langle P_\alpha J_z \rangle = \langle ^rE_+ | P_\alpha J_z | ^rE_+ \rangle \approx \langle P_\alpha \rangle \langle J_z \rangle \approx \langle P_\alpha \rangle K. \quad (6)$$

The expectation values for $\langle P_\alpha \rangle$ and $\langle P_\alpha J_z \rangle$ cannot easily be guessed at, but if all expectation values in Eq. (6) are computed from the torsion-rotation wavefunctions, then Eq. (6) can serve as a semi-quantitative check on the computation of $\langle P_\alpha J_z \rangle$.

3.3. Spin-spin interaction

As our fits got better, we found that a slight offset of a few kHz was needed to describe the difference between the average (center position) of the two outer hyperfine components and the average

of the two inner components in many low- J quartet patterns. We have empirically modeled this offset with a spin-spin interaction term of the form

$$H_{ss} = 4C_{ss} [\langle J_z^2 \rangle / J(J+1)] (\mathbf{I}_{OH} \cdot \mathbf{I}_{CH3})_{LAB} \quad (7)$$

The $(\mathbf{I}_{OH} \cdot \mathbf{I}_{CH3})_{LAB}$ operator in this term was chosen because it has matrix elements given by $(1/2)[I(I+1) - I_{OH}(I_{OH}+1) - I_{CH3}(I_{CH3}+1)]$, which has the value $+1/4$ when $I = 1$ (where $\mathbf{I} \equiv \mathbf{I}_{OH} + \mathbf{I}_{CH3}$), and the value $-3/4$ when $I = 0$. The $F = J \pm 1$ hyperfine components defined below both arise from $I = 1$ states, so their center of gravity is shifted up by $+C_{ss}[\langle J_z^2 \rangle / J(J+1)]$. One of the $F = J$ hyperfine components arises from $I = 1$, the other from $I = 0$, so the center of gravity of the two mixed $F = J$ levels is shifted down by $-C_{ss}[\langle J_z^2 \rangle / J(J+1)]$. The $\langle J_z^2 \rangle / J(J+1)$ factor was chosen empirically, since it seemed to describe the decrease observed in the experimental offset values with increasing J .

The final hyperfine Hamiltonian H_{eff} is then given by the sum of the effective spin-rotation, spin-torsion, and spin-spin Hamiltonians defined above:

$$\begin{aligned} H_{eff} = H_{sr} + H_{st} + H_{ss} = & C^{OH} (\mathbf{I}_{OH} \cdot \mathbf{J})_{LAB} + C^{CH3} (\mathbf{I}_{CH3} \cdot \mathbf{J})_{LAB} \\ & + 4C_{ss} [\langle J_z^2 \rangle / J(J+1)] (\mathbf{I}_{OH} \cdot \mathbf{I}_{CH3})_{LAB} \\ = & (C_{sr}^{OH} + C_{st}^{OH}) (\mathbf{I}_{OH} \cdot \mathbf{J})_{LAB} + (C_{sr}^{CH3} + C_{st}^{CH3}) (\mathbf{I}_{CH3} \cdot \mathbf{J})_{LAB} \\ & + 4C_{ss} [\langle J_z^2 \rangle / J(J+1)] (\mathbf{I}_{OH} \cdot \mathbf{I}_{CH3})_{LAB}. \end{aligned} \quad (8)$$

Eqs. (S-18a) to (S-18d) in [4] give the hyperfine energy levels arising from the spin-rotation operators in Eq. (8). We add the $\pm C_{ss}[\langle J_z^2 \rangle / J(J+1)]$ term arising from the empirical spin-spin interaction operator in Eq. (8) to these equations and rewrite the hyperfine splitting energies E for each F component as

$$\begin{aligned} E(F = J - 1) = & (-1/4) (C^{OH} + C^{CH3}) \\ & - (1/2) (C^{OH} + C^{CH3}) (J + 1/2) \\ & + C_{ss} [\langle J_z^2 \rangle / J(J+1)] \end{aligned} \quad (9a)$$

$$\begin{aligned} E(F = J) = & (-1/4) (C^{OH} + C^{CH3}) \\ & - (1/2) [(C^{OH} + C^{CH3})^2 (J + 1/2)^2 + C^{OH} C^{CH3}]^{1/2} \\ & - C_{ss} [\langle J_z^2 \rangle / J(J+1)] \end{aligned} \quad (9b)$$

$$\begin{aligned} E(F = J) = & (-1/4) (C^{OH} + C^{CH3}) \\ & + (1/2) [(C^{OH} + C^{CH3})^2 (J + 1/2)^2 + C^{OH} C^{CH3}]^{1/2} \\ & - C_{ss} [\langle J_z^2 \rangle / J(J+1)] \end{aligned} \quad (9c)$$

$$\begin{aligned}
 E(F=J+1) = & (-1/4)(C^{OH} + C^{CH3}) \\
 & + (1/2)(C^{OH} + C^{CH3})(J+1/2) \\
 & + C_{ss}[J_z^2/J(J+1)].
 \end{aligned}
 \quad (9d)$$

The equations finally used in our least-squares fits of observed hyperfine splittings are given by Eqs. (9a) to (9d) with the first $(-1/4)(C^{OH} + C^{CH3})$ term removed. We note in passing that when $J \gg 1$ and $C^{OH} \neq C^{CH3}$ these equations can be fully linearized in all hyperfine interaction constants by expanding the square root in Eqs. (9b) and (9c) to give Eq. (S-19) in [4], and that many of our initial fits were carried out with the linearized versions of Eq. (9).

3.4. Simple vector coupling and intensity arguments

If the combined spin-rotation and spin-torsion hyperfine splitting of one $I = 1/2$ system (either that from the $I = 1/2$ system of the hydroxyl group or that from the $I = 1/2$ system of the methyl group) is significantly larger than the hyperfine splitting from the other $I = 1/2$ system, then we can imagine, for qualitative understanding purposes, a stepwise vector coupling scheme, where we first couple the $I_1 = 1/2$ spin (with the larger splitting) to J to define an intermediate quantum number $F_1 = J \pm 1/2$ associated with $F_1 = J + I_1$. We then couple the $I_2 = 1/2$ spin (with the smaller splitting) to the two F_1 values to define the total angular momentum quantum number F associated with $F = F_1 + I_2 = J + I_1 + I_2$, obtaining $F = J + 1$ and $F = J$ from the $F_1 = J + 1/2$ level and $F = J$ and $F = J - 1$ from the $F_1 = J - 1/2$ level.

If $J \gg 1$, and if I_1 corresponds to the same spin system in the upper and lower states of a transition, then the usual $\Delta F_1 = \Delta J$ and $\Delta F = \Delta F_1$ selection rules [8] can be applied to give only four strong transitions (out of a possible 14 for a Q-branch torsion-rotation transition). We would thus expect to see hyperfine quartets in the methanol transitions under investigation here. We would also expect the lines in each quartet to be nearly symmetrically distributed (see Eq. S-19 of [4]), with the relative intensities for the lines in a given quartet pattern nearly proportional to their $2F + 1$ values.

As discussed in more detail below, we believe that hyperfine doublets arise in the $\nu_t = 1$ methanol spectrum when the four strong hyperfine lines of the quartet pattern overlap in pairs, and singlets arise when all four strong lines in the quartet pattern nearly coincide. Our explanation for the triplet patterns involves crossover resonances, which arise when the simple selection rules above are disturbed by mixing of the two levels with the same $F = J$ value, but different F_1 values.

The four energy levels obtained by vector coupling are illustrated in Fig. 1 for the $J_K = 7_{+6} \leftarrow 7_{+7}$ E-species Q-branch transition occurring in our data set. The situation is not quite as simple as described above because I_{OH} gives rise to the larger splitting in the upper state, whereas I_{CH3} gives rise to the larger splitting in the lower state. For this reason, intensities for the many formally allowed $F' \leftarrow F''$ transitions (satisfying $\Delta F = 0, \pm 1$) must be determined by numerical calculation (see below).

4. Assignment ambiguities

When hyperfine splitting patterns are observed only for relatively high J values, it is frequently impossible to unambiguously assign F values to the various splitting components. For our case, this would correspond to four observed hyperfine components in any given quartet pattern, which must each be assigned to one of the Eqs. (9a) to (9d), leading to a total of $4! = 24$ possible different assignments.

Fortunately, the present data set contains several low- J transitions where the $2F + 1 = 2J - 1, 2J + 1, 2J + 1$, and $2J + 3$ intensity

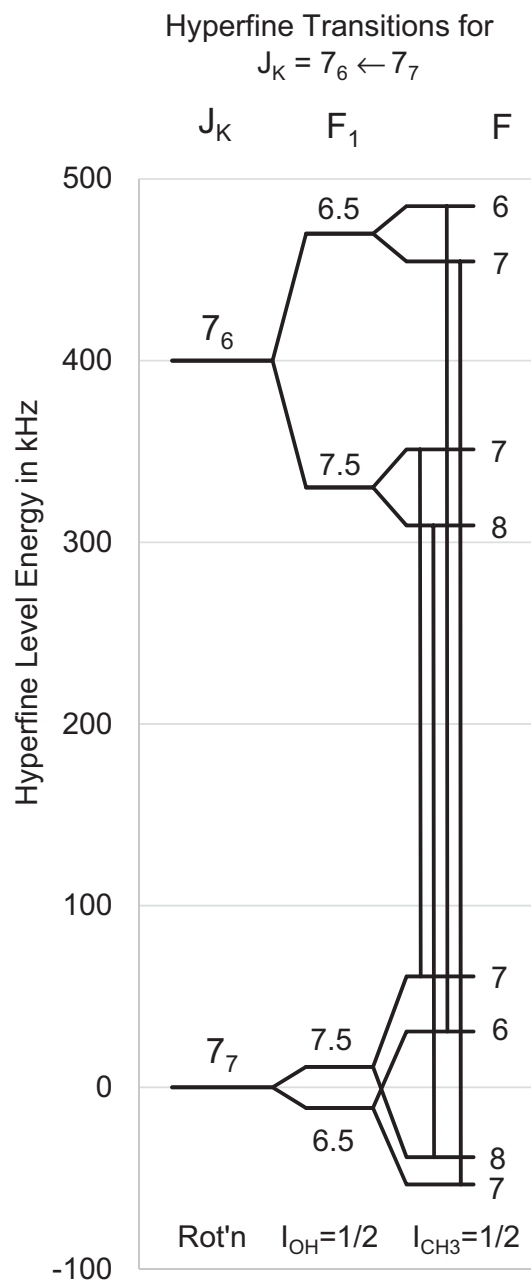


Fig. 1. An energy level diagram for the Q(7) line with $K' \leftarrow K'' = +6 \leftarrow +7$ of series (i) in Section 2. The hyperfine patterns for the lower and upper states are each drawn to scale (in kHz), but the lower and upper states without hyperfine splitting have been placed arbitrarily at 0 and 400 kHz, respectively, for ease of computer drawing. This diagram illustrates a two-step coupling scheme that can be used to understand the hyperfine levels under discussion here. The rotational angular momentum J is first coupled to the $I_{OH} = 1/2$ spin system to give an $F_1 = J + 1/2$ level and an $F_1 = J - 1/2$ level. The $F_1 = J + 1/2$ level is then coupled to the $I_{CH3} = 1/2$ spin system to give an $F = J + 1$ and an $F = J$ level. Similarly, the $F_1 = J - 1/2$ level is coupled to the $I_{CH3} = 1/2$ spin system to give an $F = J$ and an $F = J - 1$ level. The resulting energy level patterns turn out to be quite different for the $K' = +6$ and the $K'' = +7$ states. Only the four strong lines predicted by the $\Delta F = \Delta F_1 = \Delta J$ rule when $J \gg 1$ [8] are shown, in order of increasing frequency. Their relative intensities are medium, stronger, weaker, medium, respectively. (For a visual display of how internal rotation splittings can reorder K levels in $\nu_t \geq 1$ torsional states of methanol, see Fig. 1 of [9].)

factors for given J are quite clearly observable. Fig. 2 shows examples of these relative intensities for the Q(3) to Q(7) quartet lines and the R(2) line in data set (ii) of Section 2. Fig. 3 shows similar examples for the Q(7) to Q(12) quartet lines in data set (i). We have used Figs. 2 and 3 to make assignments of the $F = J \pm 1$ components,

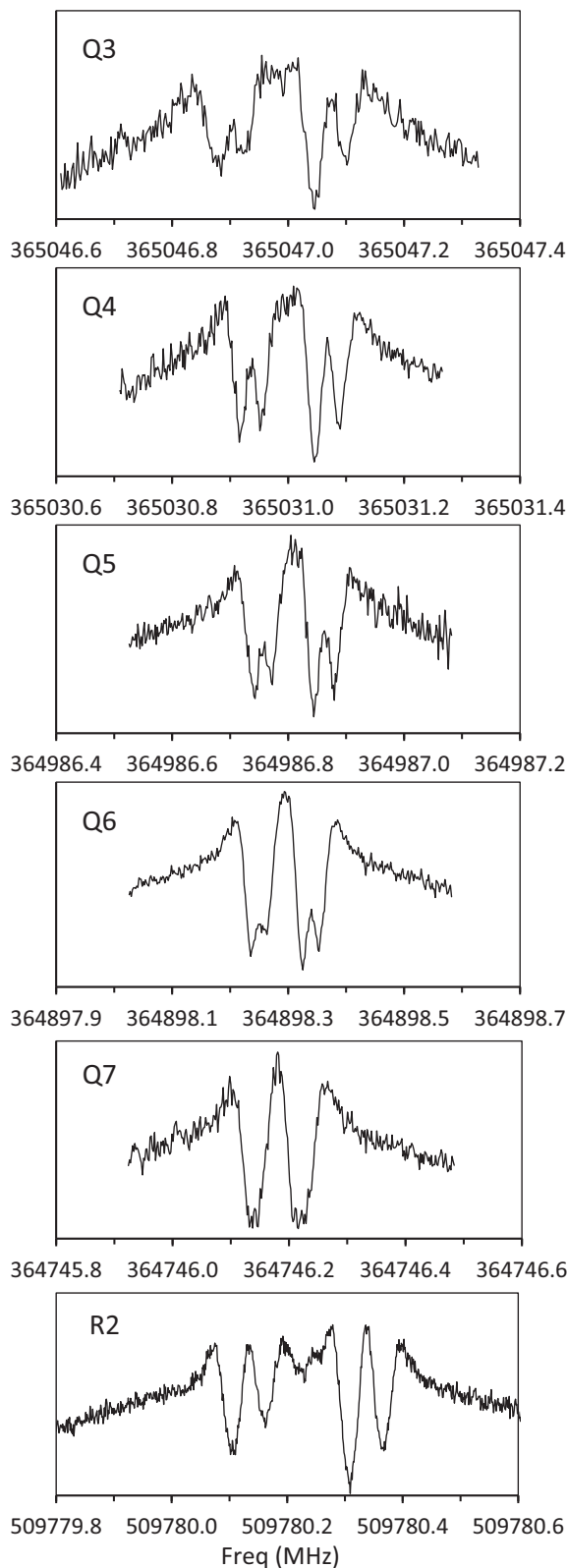


Fig. 2. The Q(3) to Q(7) and the R(2) transitions of series (ii) in Section 2, with $K' \leftarrow K'' = +3 \leftarrow +2$, showing clear intensity patterns of medium-weak-strong-medium in the quartets. We therefore assign the hyperfine components in these Q-branch patterns to $F = J, J - 1, J + 1$, and J transitions, respectively, to match the statistical weights of $2F + 1$. Fig. 2 also shows that theoretical hyperfine quartets can appear as doublets in the observed spectrum if the two lower-frequency components blend together, and the two higher-frequency components blend together, as in Q(7). We have assumed that blending of this type is the cause of all the hyperfine doublet patterns considered in this work. (For the central feature in the R(2) hyperfine pattern, see caption to Fig. 6).

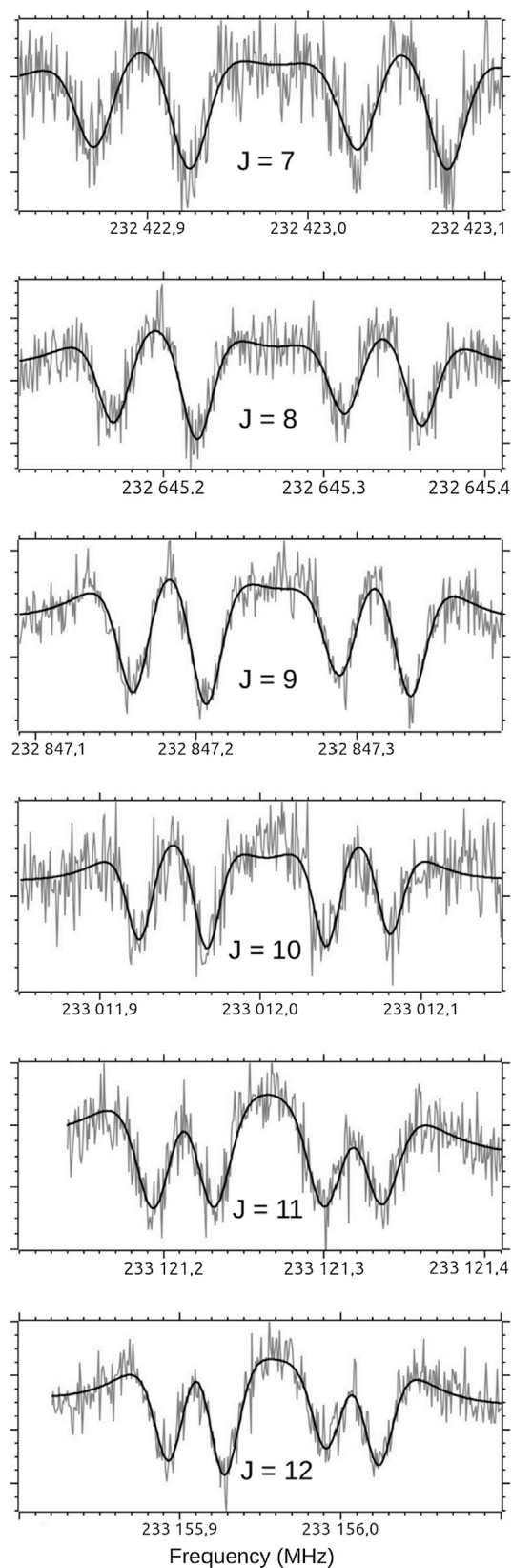


Fig. 3. The Q(7) to Q(12) transitions of series (i) in Section 2, with $K' \leftarrow K'' = +6 \leftarrow +7$, which again show clear intensity patterns. The medium-strong-weak-medium arrangement in the quartets, which differs from Fig. 2, indicates that these hyperfine components must be assigned to transitions associated with $F = J, J + 1, J - 1$, and J , respectively. An energy level diagram for the first panel (with $J = 7$) is given in Fig. 1.

i.e., the hyperfine components in Fig. 2 are assigned, in order of increasing frequency, as $F=J, J-1, J+1, J$, and those in Fig. 3 as $F=J, J+1, J-1, J$. The only remaining ambiguity is then associated with how the two $F=J$ components are to be associated with Eqs. (9b) and (9c).

This ambiguity in $F=J$ assignments turns out to be related to the fact that only the magnitude of $|C^{\text{OH}}-C^{\text{CH}_3}|$ in the square root in Eq. (9) can be determined from fits to experimental data, and not its sign. As a result, there are two sets of constants compatible with fitted values for $C^{\text{OH}}+C^{\text{CH}_3}=X$ and $|C^{\text{OH}}-C^{\text{CH}_3}|=Y>0$, namely those in Eq. (10a) or in (10b):

$$\begin{aligned} C^{\text{OH}} &= (X+Y)/2 \\ C^{\text{CH}_3} &= (X-Y)/2 \end{aligned} \quad (10a)$$

$$\begin{aligned} C^{\text{OH}} &= (X-Y)/2 \\ C^{\text{CH}_3} &= (X+Y)/2 \end{aligned} \quad (10b)$$

Changing the sign of $(C^{\text{OH}}-C^{\text{CH}_3})$ in $|C^{\text{OH}}-C^{\text{CH}_3}|$ thus leads to an exchange of all corresponding C^{OH} and C^{CH_3} hyperfine interaction constants, meaning that we cannot distinguish experimentally (as might have been anticipated) between the $I=1/2$ spin systems of the OH and CH₃ groups. Since ab initio calculations do distinguish clearly between these two spin systems, they can in principle be used to resolve this remaining assignment ambiguity.

Fig. 2 also illustrates what we believe is the origin of the doublet hyperfine patterns observed in this work. As strongly suggested by the change in the splitting patterns as we go from Q(3) down to Q(7), we have assumed that doublets arise in those quartet patterns where the two lower frequency components can no longer be resolved, and then, because of the symmetry of the pattern, the two higher frequency components can also not be resolved.

5. Least-squares fits

The 144 hyperfine splittings used in the least-squares fits are expressed as differences between the measured frequency in Table 1 for a given hyperfine component and the center of gravity of the two or four hyperfine components occurring in that pattern. Table 2 gives quantum number assignments, observed splittings, and observed-minus-calculated residuals from our best least squares fit of these data (with an unweighted standard deviation of 0.75 kHz) to six hyperfine parameters. J and K quantum number assignments for the upper and lower state are well known from the literature, e.g., [7] and references therein. F values were determined by our trial-and-error assignments and fits (see Section 4). Table S-1 in the supplemental material gives more information from the output of our final fit with some additional explanatory comments.

5.1. Computer programs used

Torsion-rotation eigenfunctions for evaluating the expectation values in Eqs. (3), (6), etc. were generated by rerunning the BELGI fits described in [7]. Each eigenfunction consists of a set of coefficients for product basis functions containing one symmetric-rotor rotational factor and one free-rotor torsional factor [4,7]. Calculations of expectation values for $J_z, J_z^2, P_z, P_z P_z$, etc. using these eigenfunctions, as well as least-squares fits of the observed hyperfine splittings to eigenvalue differences from H_{eff} , were carried out (external to BELGI) by small Mathematica or Fortran programs.

Table 2

Hyperfine assignments^a, observed splittings in kHz^b (relative to the center of gravity of the pattern in Table 1), and observed-minus-calculated (O-C) residuals in kHz from our least squares fit.

JU	FU	JL	FL	OBSERVED	O-C
$K' \leftarrow K'' = +6 \leftarrow +7$					
7	7	7	7	-110.800	-0.45
7	8	7	8	-51.300	0.54
7	6	7	6	53.400	-0.88
7	7	7	7	108.700	0.80
8	8	8	8	-96.475	0.59
8	9	8	9	-44.575	1.25
8	7	8	7	46.325	-1.39
8	8	8	8	94.725	-0.44
9	9	9	9	-86.625	-0.02
9	10	9	10	-41.525	-0.45
9	8	9	8	42.675	0.08
9	9	9	9	85.475	0.39
10	10	10	10	-78.325	-0.20
10	11	10	11	-36.825	0.43
10	9	10	9	38.275	-0.21
10	10	10	10	76.875	-0.02
11	11	11	11	-71.050	0.04
11	12	11	12	-34.250	-0.14
11	10	11	10	35.450	0.32
11	11	11	11	69.850	-0.23
12	12	12	12	-65.700	-0.54
12	13	12	13	-31.100	0.40
12	11	12	11	32.400	0.06
12	12	12	12	64.400	0.09
13	13	13	13	-59.925	0.14
13	14	13	14	-28.925	0.38
13	12	13	12	29.575	-0.43
13	13	13	13	59.275	-0.08
14	14	14	14	-55.775	-0.15
14	15	14	15	-26.675	0.76
14	13	14	13	27.025	-1.00
14	14	14	14	55.425	0.40
15	15	15	15	-52.000	-0.28
15	16	15	16	-26.000	-0.17
15	14	15	14	26.000	-0.34
15	15	15	15	52.000	0.78
$K' \leftarrow K'' = +3 \leftarrow +2$					
3	3	3	3	-108.300	0.51
3	2	3	2	-62.500	-2.44
3	4	3	4	57.700	2.03
3	3	3	3	113.100	-0.11
4	4	4	4	-83.250	1.28
4	3	4	3	-47.250	-1.30
4	5	4	5	44.750	1.43
4	4	4	4	85.750	-1.42
5	5	5	5	-68.500	0.64
5	4	5	4	-37.500	-0.27
5	6	5	6	35.500	0.03
5	5	5	5	70.500	-0.40
6	6	6	6	-57.500	0.97
6	5	6	5	-30.500	0.76
6	7	6	7	29.500	-0.50
6	6	6	6	58.500	-1.23
7	6	7	6	-39.500	-0.75
7	8	7	8	39.500	0.75
8	7	8	7	-35.000	-0.95
8	9	8	9	35.000	0.95
9	8	9	8	-31.000	-0.72
9	10	9	10	31.000	0.72
10	9	10	9	-27.500	-0.32
10	11	10	11	27.500	0.32
11	10	11	10	-24.000	0.54
11	12	11	12	24.000	-0.54
12	11	12	11	-22.500	-0.24
12	13	12	13	22.500	0.24
13	12	13	12	-20.500	-0.26
13	14	13	14	20.500	0.26
14	13	14	13	-18.500	-0.06
14	15	14	15	18.500	0.06
15	14	15	14	-16.500	0.18
15	16	15	16	16.500	-0.18

(continued on next page)

Table 2 (continued)

JU	FU	JL	FL	OBSERVED	O-C
16	15	16	15	−15.000	0.13
16	17	16	17	15.000	−0.13
$K' \leftarrow K'' = -2 \leftarrow -3$					
7	6	8	7	−16.500	0.41
7	8	8	9	16.500	−0.41
9	8	10	9	−13.500	0.05
9	10	10	11	13.500	−0.05
10	9	11	10	−12.500	−0.16
10	11	11	12	12.500	0.16
11	10	12	11	−11.500	−0.16
11	12	12	13	11.500	0.16
12	11	13	12	−10.500	−0.07
12	13	13	14	10.500	0.07
$K' \leftarrow K'' = +8 \leftarrow +7$					
8	9	8	9	−53.700	0.27
8	7	8	7	53.700	−0.27
9	10	9	10	−47.700	0.02
9	8	9	8	47.700	−0.02
10	11	10	11	−43.050	−0.19
10	9	10	9	43.050	0.19
11	12	11	12	−39.000	−0.05
11	10	11	10	39.000	0.05
12	13	12	13	−36.500	−0.77
12	11	12	11	36.500	0.77
13	14	13	14	−33.300	−0.29
13	12	13	12	33.300	0.29
14	15	14	15	−30.650	0.04
14	13	14	13	30.650	−0.04
15	16	15	16	−28.150	0.51
15	14	15	14	28.150	−0.51
16	17	16	17	−26.400	0.48
16	15	16	15	26.400	−0.48
17	18	17	18	−25.050	0.25
17	16	17	16	25.050	−0.25
18	19	18	19	−23.300	0.58
18	17	18	17	23.300	−0.58
19	20	19	20	−21.950	0.65
19	18	19	18	21.950	−0.65
20	21	20	21	−21.350	0.08
20	19	20	19	21.350	−0.08
21	22	21	22	−19.900	0.48
21	20	21	20	19.900	−0.48
22	23	22	23	−19.300	−0.18
22	21	22	21	19.300	0.18
23	24	23	24	−17.700	0.61
23	22	23	22	17.700	−0.61
24	25	24	25	−17.800	−0.36
24	23	24	23	17.800	0.36
$K' \leftarrow K'' = +6 \leftarrow +7$					
9	9	10	10	−80.650	−0.45
9	10	10	11	−41.950	0.75
9	8	10	9	42.050	−1.12
9	9	10	10	80.550	0.82
10	10	11	11	−72.900	−0.19
10	11	11	12	−38.300	0.08
10	9	11	10	38.500	−0.32
10	10	11	11	72.700	0.44
$K' \leftarrow K'' = +3 \leftarrow +2$					
3	3	2	2	−128.650	−0.23
3	2	2	1	−74.850	0.29
3	4	2	3	73.950	−0.31
3	3	2	2	129.550	0.25
$K' \leftarrow K'' = +3 \leftarrow +2$					
11	10	12	11	−24.950	−0.50
11	12	12	13	24.950	0.50
$K' \leftarrow K'' = 0 \leftarrow +1$					
2	1	1	0	−20.500	0.09
2	3	1	2	20.500	−0.09
$K' \leftarrow K'' = 0 \leftarrow +1$					
1	0	2	1	−13.000	−0.09
1	2	2	3	13.000	0.09
$K' \leftarrow K'' = -2 \leftarrow -2$					
3	4	2	3	−12.500	−0.08
3	2	2	1	12.500	0.08
$K' \leftarrow K'' = +2 \leftarrow +2$					

Table 2 (continued)

JU	FU	JL	FL	OBSERVED	O-C
3	2	2	1	−17.500	−0.16
3	4	2	3	17.500	0.16
$K' \leftarrow K'' = -1 \leftarrow -1$					
2	1	1	0	−21.650	−2.97
2	3	1	2	21.650	2.97
$K' \leftarrow K'' = +3 \leftarrow +4$					
17	16	18	17	−8.650	−2.02
17	18	18	19	8.650	2.02
$K' \leftarrow K'' = 0 \leftarrow +1$					
1	0	1	0	−20.000	1.55
1	2	1	2	20.000	−1.55

^a J and K quantum numbers for the (u)pper and (l)ower states are from the literature [7] and references therein. F quantum numbers were assigned by intensity variation and/or iterative trial-and-error fits.

^b Even though experimental measurements within a given hyperfine pattern have a relative uncertainty of 0.5 to 1 kHz (see Table 1), we present differences from the center of gravity of the hyperfine pattern to three decimal places in the “observed” column of this table to minimize round-off errors during the data processing.

5.2. Molecular constants

The six molecular constants used in our best fit are given in Table 3. The three unused constants from Eq. (2b) are those found in the quantity C_{sr}^{CH3} . (Note that we cannot choose between operators with the superscript OH and operators with the superscript CH3 based on the quality of the fit. It is necessary to make this choice based on ab initio calculations, as described in Section 6.) By properly manipulating the linearized expressions for the energy levels in Eq. (9) that are given in Eq. (S-19) of [4], it is possible to conclude that if all hyperfine patterns were doublets (i.e., no quartets were observed), then it would be nearly impossible to determine the smaller partner of each of the three pairs of constants in Eqs. (2a) and (2b), (i.e., the smaller partner of the zz pair, the xx - yy pair, or the $xx + yy + zz$ pair). Our data set has more doublet patterns than quartets, and it is indeed these three smaller partners that were not used in Table 3.

We note in passing, that the dominant hyperfine splitting mechanism for the large splittings observed in our earlier work on $v_t = 0$ E states is completely different from the mechanism giving the large splittings observed in $v_t = 1$ E states. This is reflected in the fact that the $v_t = 0$ splittings in [4] increase approximately proportional to J as J increases, whereas the $v_t = 1$ splittings in the present work decrease approximately proportional to $1/J$ as J increases.

5.3. Quality of the fit

The three largest constants in Table 3 are determined to better than 1%, but the three smaller constants have standard errors [10] of about 10%. Increasing the number of parameters does not significantly decrease σ , but it noticeably increases the standard-error values for the molecular constants.

If we consider the fact that n hyperfine components for a given torsion-rotation transition give rise to only $n-1$ independent hyperfine splittings (which is what we are fitting), then the ratio of (independent splittings)/(hyperfine parameters) = $88/6 \approx 14.7$ splittings/parameter. This ratio is not outstandingly large, but it is large enough to suggest that the model adopted here is not being used to carry out a “random” fit of the observables.

The standard deviation of this fit is less than 1 kHz, which we believe is equal to measurement error.

Table 3

Molecular constants (in kHz) from our best least-squares fit of 144 hyperfine components to 6 parameters and comparison with experimental and theoretical values from the literature [2,3]

	Parameter	Present fit		Literature	
		RAM ^a	IAM ^b	[2]	[3]
Spin-Torsion	C_{zz}^{OH}	−65.10(13)	−65.10	69.29 ^c	11.20 ^c
	C_{zz}^{CH3}	13.432(62)	13.432		13.59 ^c
Spin-Rotation	C_{zz}^{OH}	−62.61(32)	C_{zz}^{OH} −11.79	−12.88 ^d	13.31 ^d
	C_{xx}^{OH}	1.44(15)	C_{xx}^{OH} −0.48	−0.74 ^d	0.66 ^d
	C_{yy}^{OH}		C_{yy}^{OH} −3.36	−2.85 ^d	2.94 ^d
	$C_{xx+yy+zz}^{OH}$	−1.92(18)			
Spin-Spin ^e	C_{ss}	−5.27(57)			

^a RAM constants are from our fit in Table 2 (and Table S-1 of the supplemental material) with one standard deviation (type A, coverage $k = 1$ [10]) in parentheses.

^b IAM constants are obtained from RAM values as described in Section 6. In particular, the large difference between the RAM and PAM values for C_{zz}^{OH} arises from Eq. (12).

^c Values from fits in [2,3]. Only magnitudes can be compared because of differences in phase convention choices.

^d Ab initio values from [2,3]. Only magnitudes can be compared. Ab initio values for spin-torsion constants cannot be calculated from commercial packages at present.

^e A spin-spin interaction constant introduced empirically via Eq. (7), with no theoretical derivation.

6. Comparison of RAM molecular constants with other values in the literature

6.1. Influence of the torsional angular momentum expectation value $\langle P_\alpha \rangle$ on the magnitude of spin-torsion coupling in the $v_t = 0$ and 1 states of methanol

The $v_t = 1$ E state is just below the top of the barrier in methanol, so it is much closer to the free internal-rotation limit than the $v_t = 0$ A and E states are. One simple picture of spin-rotation interaction visualizes it as the interaction of a nuclear-spin magnet with the magnetic field generated by electric currents associated with the closed-circuit angular motion of nuclear and electronic charges in the rotating molecule [8]. We thus expected, and we believe we have found, that the nearly-free internal-rotation effects lead to much larger spin-torsion coupling constants in the $v_t = 1$ E state (e.g., the value of $C_{zz}^{OH} \approx -65$ kHz in Table 3) than can be seen in the torsional $v_t = 0$ E state.

The two spin-torsion operators used in the present work are each of the form $I_z P_\alpha$, where the molecule-fixed z component of the nuclear spin operator I_z and the torsional angular momentum operator P_α are both of symmetry species A_2 in methanol (see Table 1 of [4]). One is thus tempted to first take an average over the torsional and rotational variables, and then to consider an expression of the form $I_z \langle P_\alpha \rangle$. However, as briefly explained in Section 3.1 of [7], there are in fact several different coordinate systems in use for treating molecules with methyl-top internal rotation [11], and these different coordinate systems lead to different physical interpretations for the torsional angular momentum operator $P_\alpha \equiv -\hbar \partial / \partial \alpha$. For most molecular spectroscopists, intuitive thinking works best in an Eckart axis system [12], where Coriolis interaction between the vibrational angular momentum and overall rotation has been eliminated to first order, and it is in fact the Internal-Axis-Method (IAM) coordinate system [11] that corresponds to an Eckart axis system, rather than the Rho-Axis-Method (RAM) coordinate system used to carry out the least-squares fits in [7].

Roughly speaking, the IAM torsional Hamiltonian has the form of Eq. (11a), whereas the RAM torsional Hamiltonian has the form of Eq. (11b) [11].

$$H_{\text{torsion}} = F(P_\alpha^{\text{IAM}})^2 + (1/2)V_3(1 - \cos 3\alpha) \quad (11a)$$

$$H_{\text{torsion}} = F(P_\alpha^{\text{RAM}} \pm \rho J_z)^2 + (1/2)V_3(1 - \cos 3\alpha) \quad (11b)$$

where RAM treatments with both the + and the − sign are in use in the literature (to maintain continuity with earlier papers on any given molecule). Whereas the minus sign is to be preferred [13], tradition requires the plus sign for methanol (see footnote b of Table 2 of [7]), which then leads to the operator equation

$$P_\alpha^{\text{IAM}} = P_\alpha^{\text{RAM}} + \rho J_z. \quad (12)$$

Table 4 shows expectation values for the three operators J_z , P_α^{RAM} , and P_α^{IAM} in the $J = K$ torsion-rotation state for both $v_t = 0$ and $v_t = 1$. Expectation values for the first two operators are calculated directly from the torsion-rotation eigenfunctions obtained in [7], and $\langle P_\alpha^{\text{IAM}} \rangle$ is calculated using Eq. (12). The expectation values $\langle J_z \rangle$ in Table 4 are integers to two decimal places, and they thus serve to define the K value of each torsion-vibration state. (The J value is defined exactly when setting up the Hamiltonian matrices.) Knowledge of the K values then fixes the $v_t = 0$ and $v_t = 1$ labels of the eigenvectors, and therefore the $\langle P_\alpha \rangle_{v_t=0}$ and $\langle P_\alpha \rangle_{v_t=1}$ labels. Table 4 shows that values for $\langle P_\alpha^{\text{RAM}} \rangle$ tend to increase linearly with $\langle J_z \rangle$ (apart from some superimposed sinusoidal variation with K [11]), and that these expectation values for $v_t = 0$ and $v_t = 1$ are not strikingly different. On the other hand, values of $\langle P_\alpha^{\text{IAM}} \rangle_{v_t=0}$ (for which the ρJ_z contribution is absent) do not rise above 0.25h, (where we have added the usually omitted \hbar to indicate that these expectation values are in units of angular momentum). In contrast, values of $\langle P_\alpha^{\text{IAM}} \rangle_{v_t=1}$ reach values of nearly 2h. These IAM expectation values are in keeping with our intuitive ideas that: (i) significantly more torsional angular momentum is generated in a $v_t = 1$ E-species state (near the top of the barrier) than in a $v_t = 0$ E-species state (rather far down in the well), and (ii) this increased torsional angular momentum corresponds to an increased torsional angular velocity, and thus to an increased torsional magnetic field, and thus finally to an increased spin-torsion hyperfine interaction in $v_t = 1$ E-species states, compared to $v_t = 0$.

6.2. Numerical comparison of our fitted molecular constants with values in the literature

Table 3 contains values for our fitted parameters, which multiply operators like $P_\alpha^{\text{RAM}} J_z$, J_z^2 , $J_x^2 - J_y^2$, and J^2 (see Section 3). To compare these parameters with ab initio calculations in the literature, we need to take linear combinations of them as follows, where the notation on the left is from Tables 6 and 8 of [2], and the notation on the right is from Table 3.

$$\begin{aligned} C_{xx}^{0,h} &= C_{xx+yy+zz}^{OH} + C_{xx-yy}^{OH} \\ C_{yy}^{0,h} &= C_{xx+yy+zz}^{OH} - C_{xx-yy}^{OH} \\ C_{zz}^{0,h} &= C_{xx+yy+zz}^{OH} + C_{zz}^{OH} - \rho C_{zz}^{OH} \\ S_z^{0,h} &= C_{zz}^{OH} \\ S_z^0 &= C_{zz}^{CH3} \end{aligned} \quad (13)$$

The first two equations can be obtained simply by collecting all coefficients that multiply the individual xx or yy angular momentum operators. Obtaining the third equation requires more

Table 4

Expectation values for the z component of the rotational angular momentum $\langle J_z \rangle^a$ and for the torsional angular momentum $\langle p_\alpha^{\text{RAM}} \rangle^a$ in the Rho-Axis-Method (RAM) [7,10] used here, as well as for the torsional angular momentum $\langle p_\alpha^{\text{IAM}} \rangle^b$ in the Internal-Axis-Method (IAM) [7,10], for the lowest $J = K$ torsion-rotation states with $v_t = 0$ and $v_t = 1$ in methanol.

$v_t = 0$ $\langle J_z \rangle$	$v_t = 0$ $\langle p_\alpha^{\text{RAM}} \rangle$	$v_t = 0$ $\langle p_\alpha^{\text{IAM}} \rangle$	$v_t = 1$ $\langle J_z \rangle$	$v_t = 1$ $\langle p_\alpha^{\text{RAM}} \rangle$	$v_t = 1$ $\langle p_\alpha^{\text{IAM}} \rangle$
−8.00	+6.67	+0.19	−8.00	+4.62	−1.86
−7.00	+5.76	+0.09	−7.00	+5.26	−0.41
−6.00	+4.62	−0.24	−6.00	+6.25	+1.38
−5.00	+4.03	−0.03	−5.00	+4.62	+0.57
−4.00	+3.48	+0.23	−4.00	+1.69	−1.55
−3.00	+2.39	−0.04	−3.00	+2.60	+0.17
−2.00	+1.40	−0.22	−2.00	+3.37	+1.75
−1.00	+0.89	+0.08	−1.00	−0.88	−1.69
0.00	+0.22	+0.22	0.00	−1.13	−1.13
+1.00	−0.97	−0.16	+1.00	−0.08	+0.73
+2.00	−1.77	−0.15	+2.00	+0.33	+1.95
+3.00	−2.26	+0.17	+3.00	−4.36	−1.93
+4.00	−3.10	+0.14	+4.00	−3.86	−0.61
+5.00	−4.28	−0.23	+5.00	−2.83	+1.22
+6.00	−4.92	−0.06	+6.00	−3.39	+1.47
+7.00	−5.44	+0.23	+7.00	−7.35	−1.68
+8.00	−6.46	+0.02	+8.00	−6.53	−0.05

^a Calculated from eigenfunctions generated from molecular constants of the least-squares fit in Ref. [7]. The K value for each state is equal to the integer nearest to $\langle J_z \rangle$.

^b Calculated from the relation $\langle p_\alpha^{\text{IAM}} \rangle = \langle p_\alpha^{\text{RAM}} \rangle + \rho \langle J_z \rangle$ (see Section 3.1 of [7]).

thought, because ab initio calculations are (implicitly) carried out in an Eckart (IAM) system [12], whereas our fitting is done with matrix elements evaluated in the RAM system. We therefore use Eq. (12) to obtain a correspondence between various fitted (RAM) parameters in Table 3 and the two IAM parameters $c_{zz}^{0,h}$ and $s_z^{0,h}$ (in the notation of [2]):

$$\begin{aligned}
 C_{zz}^{\text{OH}}(p_\alpha^{\text{RAM}})J_z + (C_{xx+yy+zz}^{\text{OH}} + C_{zz}^{\text{OH}})J_z^2 \\
 = C_{zz}^{\text{OH}}(p_\alpha^{\text{IAM}} - \rho J_z)J_z + (C_{xx+yy+zz}^{\text{OH}} + C_{zz}^{\text{OH}})J_z^2 \\
 = C_{zz}^{\text{OH}}(p_\alpha^{\text{IAM}})J_z + (C_{xx+yy+zz}^{\text{OH}} + C_{zz}^{\text{OH}} - \rho C_{zz}^{\text{OH}})J_z^2 \\
 = s_z^{0,h}(p_\alpha^{\text{IAM}})J_z + c_{zz}^{0,h}J_z^2.
 \end{aligned} \quad (14)$$

Equations for other quantities with superscript CH3 could be included in Eq. (13), but they are not needed because we could not determine those parameters in the present work.

The right side of Table 3 compares values for our fitted spin-rotation and spin-torsion coupling constants (after conversion using Eq. (13)) with their ab initio counterparts or their fitted values from [2,3].

We believe that our fitted values for the three IAM spin-rotation constants along the principal axes in Table 3 agree well with ab initio values for the hydroxyl proton from both theoretical papers [2,3], especially because the small number of constants that we could reasonably fit to our limited experimental data inevitably leads to “effective values” for the experimentally fitted constants. (In fact, our fitted values for the xx and zz components of the spin-rotation constant also agree well with the ab initio xx and zz values for the methyl protons, but our yy component of $−3.4$ kHz is significantly larger in magnitude than the ab initio value [2,3] of approximately 0.7 kHz for the methyl protons.)

Unfortunately, our fitted values for the two spin-torsion constants s in Table 3 cannot be compared with ab initio values, because the electronic contribution to spin-torsion constants cannot be obtained from presently available quantum chemistry software packages [2,3]. Our fitted values can be compared, however, with fitted values from [2,3], and this comparison shows somewhat random agreement and disagreement. Our value for $s_z^{0,h}$

agrees well with the value from [2], but disagrees with the value from [3]. Our value for s_z^0 agrees well with the value from [3]. Some disagreement is not too surprising, since different data sets and different sets of constants are being fitted here and in [2,3].

7. Hyperfine patterns with a weak central component

Fig. 4 shows hyperfine patterns for the Q(8) to Q(13) transitions of series (iv), where a weak central feature is clearly visible in the lower J patterns. An energy level diagram for the Q(8) transition is shown in Fig. 5, drawn approximately to scale for the hyperfine splittings measured in kHz, but not to scale for the torsion-rotation transition frequency measured in GHz. Transitions are ordered by decreasing upper state J . The four strong $\Delta F = \Delta J = \Delta F_1$ transitions are shown as solid lines. Two weaker transitions with $\Delta F = \Delta J \neq \Delta F_1$ are shown as dashed lines. Table 5 gives Lamb-dip frequencies (relative to the center of gravity of the four strongest lines) of these six hyperfine transitions for the Q(8) line shown in Fig. 5, calculated from our final set of molecular constants, as well as relative intensities for those transitions, calculated using the procedure of Section S-B of [4], as described in Section S-2 of the supplemental material. The six transitions in Table 5 form the two outer components of the Q(8) Lamb-dip spectrum shown in Fig. 4, where each component contains three unresolved transitions.

Since none of the six strong or moderately strong transitions in Fig. 5 give rise to an absorption feature at the center of the hyperfine pattern, we consider next the possibility of three-level Λ -type crossover resonances [14]. A crossover resonance cannot be indicated as a normal transition because it occurs at a frequency obtained by averaging the frequencies of the left (solid) leg and the right (dashed) leg of a given Λ shape (with a given $J = 8$ upper state) in Fig. 5. The close-lying $F = J$ levels near the center of the upper state splitting pattern in Fig. 5 are particularly well suited to generating two overlapping crossover resonance signals near the center of the Lamb-dip hyperfine pattern, since one of the Λ diagrams leads to an absorption at $−4.6$ kHz, the other at $+6.8$ kHz, giving a blended doublet centered near $+1.1$ kHz.

Changing the meaning of the letter I from nuclear spin to intensity for this section, we calculate the crossover intensity using the approximate expression $I_c = [I_s I_w]^{1/2}$ [15,16], where I_c is the intensity of the crossover resonance, and I_s and I_w are the intensities of the stronger and weaker transitions in a given Λ diagram. Summing the intensities of all overlapping lines within each component of the triplet, we calculate a ratio of total crossover intensity to average intensity of the two outer triplet components of 0.45, 0.36, 0.27, and 0.21 for the Q(8) to Q(11) triplet patterns in Fig. 4, respectively. These ratios indicate that the central component in Fig. 4 should gradually disappear as J increases, in agreement with what is observed.

For comparison of calculations with experiment, we measured the line intensities in Fig. 4 by curve-fitting the three components. To improve the poor signal-to-noise ratio often observed in Lamb-dip spectra, we averaged many individual records. Because the total averaging time for some records reached 20 h, the width of each Lamb-dip scan was limited to some minimum acceptable value. This made it impossible to determine correctly the experimental Doppler broadened profile, so the Doppler width was fixed at a calculated value (using the common formula based on absolute temperature and molecular weight). The intensity of the scanned portion of the Doppler profile, as well as intensities of the Lamb-dip components, were then determined by fitting the experimental records. Such an approach is not very precise (compared to direct measurements), but in our case it was the only practical method available to obtain the desired relative-intensity data. Measure-

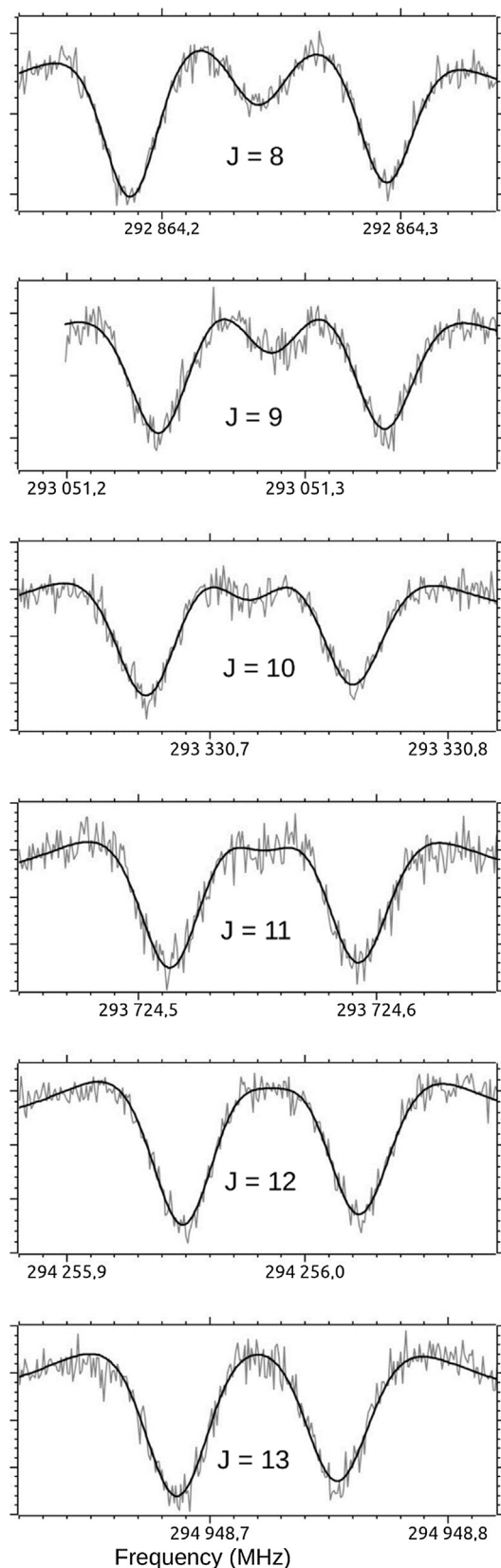


Fig. 4. The Q(8) to Q(13) transitions of series (iv) in Section 2, with $K' \leftarrow K'' = +8 \leftarrow +7$. The first few lines in this series are clearly triplets. We ascribe each of the strong outer components to the overlap of two of the four expected strong hyperfine transitions. We ascribe the weak central component to crossover resonances involving the $F = J$ levels (see Section 7 and Fig. 5).

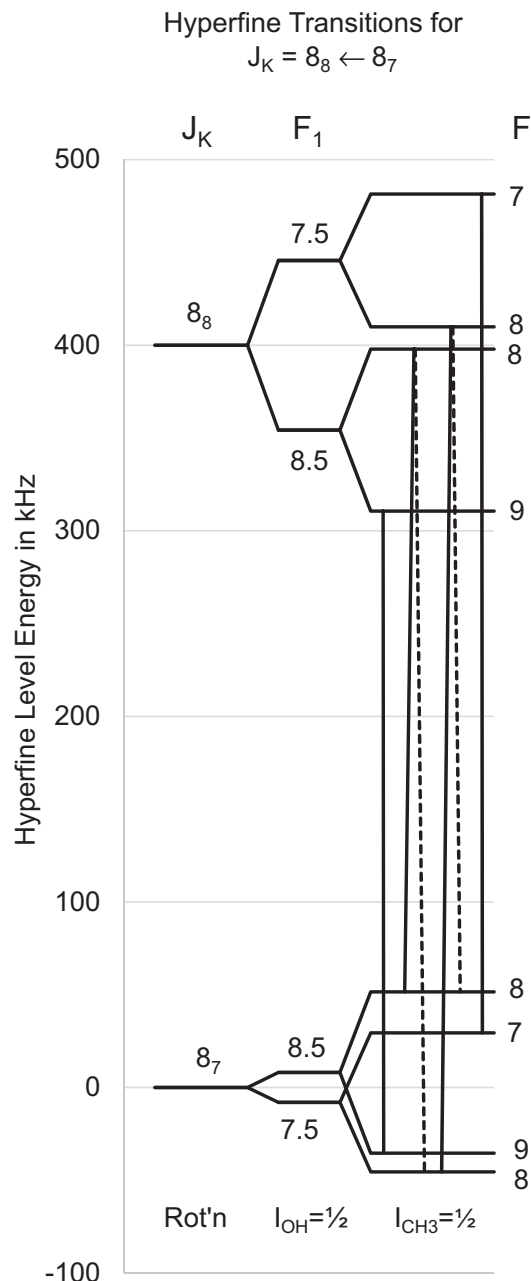


Fig. 5. An energy level diagram for the Q(8) line with $K' \leftarrow K'' = +8 \leftarrow +7$ of series (iv) in Section 2. See caption to Fig. 1 for scale. This diagram illustrates the Λ -type crossover-resonance origin of the weak central features present in the first few lines of this series. The Λ diagram on the left gives rise to a crossover resonance at -4.6 kHz in the hyperfine splitting pattern, that on the right gives a resonance at $+6.8$ kHz. See Section S-2 of the supplemental material for a discussion of the relative intensities of the observed triplet components of this transition.

ments of this type give experimental intensity ratios of the central component to the average of the two outer components of 0.42, 0.49, 0.39, and 0.31. We believe that the near agreement of these experimental ratios with their calculated values supports our assignment of the weak central features in the triplets in Fig. 4 to crossover resonances.

The R(2) transition shown in Fig. 2 also has a weak central component, but for this transition, the hyperfine splittings of the upper and lower torsion-rotation states of the R(2) transition shown in Fig. 6 suggest that the central component represents a blend of many components, as described in more detail in Section S-2.

Table 5Calculated frequencies (in kHz)^a and relative intensities^b for the Q(8) hyperfine components shown in Fig. 5^c

F_1	F'	F''_1	F''	ν_{hf}^a	Intensity ^b	Line ^c
8.5	9	8.5	9	−54.2	1.27	Solid
8.5	8	8.5	8	−53.7	0.82	Solid
8.5	8	7.5	8	+44.5	0.33	Dashed
7.5	8	7.5	8	+55.9	0.81	Solid
7.5	8	8.5	8	−42.3	0.31	Dashed
7.5	7	7.5	7	+52.0	1.00	Solid

^a From the RAM constants in Table 3. These six transitions form a doublet, with components displaced about −54 kHz and +54 kHz from the center in the first panel of Fig. 4.

^b From the procedure in Section S-B of [4], as described in Section S-2.

^c Transitions in this table are ordered from high F to low F . Solid lines in Fig. 5 represent the four strong $\Delta F = \Delta J = \Delta F_1$ transitions. Dashed lines represent the two weaker $\Delta F = \Delta J \neq \Delta F_1$ transitions.

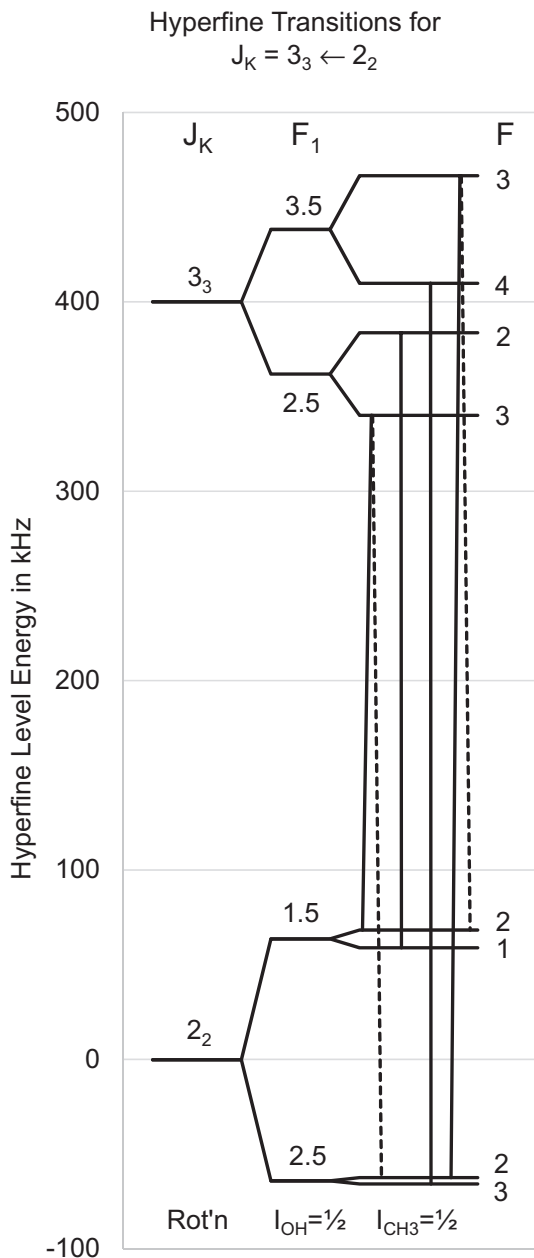


Fig. 6. An energy level diagram for the R(2) line in Fig. 2, with $K' \leftarrow K'' = +3 \leftarrow +2$. See caption to Fig. 1 for scale. This diagram illustrates the fact that the origin of the central feature in Fig. 2 is not a pair of crossover resonances analogous to those in Fig. 5, since the sum of the solid and dashed legs of the two Λ diagrams shown give crossover resonances near −63 kHz and +64 kHz, respectively and these resonances are not resolved from two of the main Lamb-dip signals near ± 75 kHz. The origin of the central feature in R(2) is explained in Section S-2 of the supplemental material.

Briefly (based on our calculations), three weak $\Delta F \neq \Delta J$ hyperfine transitions within the R(2) torsion-rotation transition contribute 0.12 to the relative intensity of the central component, and two crossover resonances contribute another 0.44.

8. Summary and outlook

In this and our previous paper [4] we considered only E-species torsion-rotation states, since these provide the most dramatic examples of large magnetic-dipole hyperfine splittings in methanol. We believe that our fits using hyperfine Hamiltonians containing empirically chosen spin-rotation, spin-torsion, and spin-spin interaction terms have qualitatively identified and quantitatively characterized the rather different causes of these large splittings in the $\nu_t = 0$ and $\nu_t = 1$ torsional E states.

At some point it will be appropriate to carry out a global fit of all observed hyperfine splittings in methanol. However, there seem to be very few large splittings in states of A symmetry (which involve $I_{\text{CH}_3} = 3/2$). Furthermore, as mentioned above, there are several tens of hyperfine parameters to be determined. It thus seems likely that a reliable global hyperfine fit of experimental hyperfine data for methanol will not be possible without a significant increase in resolution for the Lamb-dip measurements.

Our postulated Λ -type crossover resonances represent only an ad hoc initial attempt to explain unexpected intensity at the center of some of the hyperfine Lamb-dip patterns. Confirmation of this crossover-mechanism explanation will require a campaign of experimental searches for other (presumably weak) crossover resonances coupled with additional theoretical predictions of position and intensity. Higher resolution Lamb-dip measurements capable of showing the six predicted components (at least partly resolved) at −54, −42, −5, +7, +45, and +54 kHz in Q(8) of Fig. 4 and Table 5 would also be useful.

Although our search in acetaldehyde [17] for measurably large hyperfine splittings analogous to those found in methanol was not successful, we plan to search also for such splittings in methyl mercaptan.

Acknowledgments

LHX acknowledges financial support from the Natural Sciences and Engineering Research Council of Canada. SPB and GYG acknowledge funding from the Ministry of Science and Higher Education of the Russian Federation and the Russian Foundation for Basic Research: experimental data were obtained within project 0035-2019-0016 and preliminary analysis of the spectra were supported by project 18-02-00705. EAA gratefully acknowledges financial support from Centre National de la Recherche Scientifique (CNRS, France) and from Université de Lille (France). LHX and JTH are greatly indebted to Prof. H. Sasada and Ms S. Okuda for detailed

and helpful discussions of crossover resonances at several international meetings.

Appendix A. Supplementary material

Supplementary data associated with this article can be found, in the online version, at <https://doi.org/10.1016/j.jms.2018.12.003>.

References

- [1] G.Yu. Golubiatnikov, S.P. Belov, A.V. Lapinov, Paper MF04 “CH₃OH sub-doppler spectroscopy,” and S.P. Belov, A.V. Burenin, G.Yu. Golubiatnikov, A.V. Lapinov, Paper FB07 “What is the nature of the doublets in the E-methanol Lamb-dip spectra?” International Symposium on Molecular Spectroscopy, The Ohio State University, 2013.
- [2] L.H. Coudert, C. Gutlé, T.R. Huet, J.-U. Grabow, S.A. Levshakov, Spin-torsion effects in the hyperfine structure of methanol, *J. Chem. Phys.* 143 (2015). 044304-1-12.
- [3] B. Lankhaar, G.C. Groenenboom, Ad van der Avoird, Hyperfine interactions and internal rotation in methanol, *J. Chem. Phys.* 145 (2016). 244301-1-15. Erratum: *J. Chem. Phys.* 148 (2018) 149901.
- [4] S.P. Belov, G.Yu. Golubiatnikov, A.V. Lapinov, V.V. Ilyushin, E.A. Alekseev, A.A. Mescheryakov, J.T. Hougen, Li-Hong Xu, Torsionally mediated spin-rotation hyperfine splittings at moderate to high *J* values in methanol, *J. Chem. Phys.* 145 (2016). 024307-1-20.
- [5] O. Zakharenko, R.A. Motiyenko, L. Margulès, T.R. Huet, Terahertz spectroscopy of deuterated formaldehyde using a frequency multiplication chain, *J. Mol. Spectrosc.* 317 (2015) 41–46.
- [6] G.Yu. Golubiatnikov, S.P. Belov, I.I. Leonov, A.F. Andriyanov, I.I. Zinchenko, A.V. Lapinov, V.N. Markov, A.P. Shkayev, A. Guarnieri, Precision sub-Doppler millimeter and submillimeter Lamb-dip spectrometer, *Radiophys. Quantum Electron* 56 (2014) 599–609 [*Izvestiya Vuzov Radiofizika* 56 (2013) 666-677 (in Russian)].
- [7] Li-Hong Xu, J. Fisher, R.M. Lees, H.Y. Shi, J.T. Hougen, J.C. Pearson, B.J. Drouin, G. A. Blake, R. Braakman, Torsion-rotation global analysis of the first three torsional states ($v_t = 0, 1, 2$) and terahertz database for methanol, *J. Mol. Spectrosc.* 251 (2008) 305–313.
- [8] C.H. Townes, A.L. Schawlow, *Microwave Spectroscopy*, McGraw-Hill, 1955.
- [9] Li-Hong Xu, J.T. Hougen, Global fit of torsional-rotational transitions in the ground and first excited torsional states of methanol, *J. Mol. Spectrosc.* 173 (1995) 540–551.
- [10] B.N. Taylor, C.E. Kuyatt, Guidelines for evaluating and expressing the uncertainty of NIST measurement results, 1994. <http://physics.nist.gov/TN1297>.
- [11] J.T. Hougen, I. Kleiner, M. Godefroid, Selection rules and intensity calculations for a C_s asymmetric top molecule containing a methyl group internal rotor, *J. Mol. Spectrosc.* 163 (1994) 559–586.
- [12] E.B. Wilson, J.C. Decius, P.C. Cross, *Molecular Vibrations*, McGraw-Hill, 1955.
- [13] C.C. Lin, J.D. Swalen, Internal rotation and microwave spectroscopy, *Rev. Mod. Phys.* 31 (1959) 841–892.
- [14] W. Demtröder, *Laser Spectroscopy, Vol. 2, Experimental Techniques*, Fourth ed., Springer, Heidelberg, 2008.
- [15] G. Magerl, W. Schupita, J.M. Frye, W.A. Kreiner, T. Oka, Sub-Doppler spectroscopy of the v_2 band of NH₃ using microwave modulation sidebands of CO₂ laser lines, *J. Mol. Spectrosc.* 107 (1984) 72–83.
- [16] S. Okuda, H. Sasada, Intensity of a crossover signal relative to Lamb dips observed in Stark spectroscopy of methane, *J. Mol. Spectrosc.* 352 (2018) 10–15.
- [17] Li-Hong Xu, E.M. Reid, B. Guislain, J.T. Hougen, E.A. Alekseev, I. Krapivin, Ab initio calculations of torsionally mediated hyperfine splittings in E states of acetaldehyde, *J. Mol. Spectrosc.* 342 (2017) 116–124.